Front. Mech. Eng. 2022, 17(4): 31
https://doi.org/10.1007/s11465-022-0687-1

RESEARCH ARTICLE

Development of a masticatory robot using a novel cable-driven linear actuator with bidirectional motion

Haiying WEN[a,b], Jianxiong ZHU[a,b], Hui ZHANG[a,b], Min DAI[a], Bin LI[c], Zhisheng ZHANG (✉)[a], Weiliang XU (✉)[d], Ming CONG[e]

[a] *School of Mechanical Engineering, Southeast University, Nanjing 211189, China*
[b] *Engineering Research Center of New Light Sources Technology and Equipment, Ministry of Education, Nanjing 210009, China*
[c] *Department of Stomatology, Zhongda Hospital Affiliated to Southeast University, Nanjing 210009, China*
[d] *Department of Mechanical & Mechatronics Engineering, The University of Auckland, Auckland 1142, New Zealand*
[e] *School of Mechanical Engineering, Dalian University of Technology, Dalian 116024, China*

✉ *Corresponding author. E-mails: oldbc@seu.edu.cn (Zhisheng ZHANG); p.xu@auckland.ac.nz (Weiliang XU)*

ABSTRACT Masticatory robots are an effective *in vitro* performance testing device for dental material and mandibular prostheses. A cable-driven linear actuator (CDLA) capable of bidirectional motion is proposed in this study to design a masticatory robot that can achieve increasingly human-like chewing motion. The CDLA presents remarkable advantages, such as lightweight and high stiffness structure, in using cable amplification and pulley systems. This work also exploits the proposed CDLA and designs a masticatory robot called Southeast University masticatory robot (SMAR) to solve existing problems, such as bulky driving linkage and position change of the muscle's origin. Stiffness analysis and performance experiment validate the CDLA's efficiency, with its stiffness reaching 1379.6 N/mm (number of cable parts $n = 4$), which is 21.4 times the input wire stiffness. Accordingly, the CDLA's force transmission efficiencies in two directions are 84.5% and 85.9%. Chewing experiments are carried out on the developed masticatory robot to verify whether the CDLA can help SMAR achieve a natural human-like chewing motion and sufficient chewing forces for potential applications in performance tests of dental materials or prostheses.

KEYWORDS masticatory robot, cable-driven, linear actuator, parallel robot, stiffness analysis

1 Introduction

Cable and pulley systems are a widely used force transmission and amplification tool that has been applied to cranes [1], exercise machines [2], and *XY* positioning systems [3]. Cable and pulley systems have been increasingly used in robots in recent years. The end effector or link of a cable-driven parallel manipulator (CDPM) is directly driven by cables. The cable transmission allows the heavy motor to be placed at the proximal part and transmit the motion to the distal part [4,5]. Therefore, the CDPM presents the advantages of low structural weight, low inertia, and ample workspace [6] to improve the acceleration capability and reduce the entire system's energy consumption. Hence, the CDPM shows several application prospects, including high-speed pick-and-place robots [7] and large-workspace parallel 3D printers [8]. The CDPM has been increasingly used in exoskeleton and rehabilitation devices [9,10], steerable catheter [11], and bio-inspired robots, that is, humanoid necks [12,13] and robotic arms [14], given the satisfactory compliance of utilizing cables in the joint construction.

However, CDPMs present some disadvantages as in practical applications. The cable-driven link of the CDPM shows lower stiffness than the traditional rigid link that leads to control difficulties and ultimately a decrease in the robot's payload if the cable deformation becomes large. Low stiffness also affects the positioning accuracy and force distribution of the CDPM [15]. Additionally, the cable-driven system demonstrates an essential characteristic of only being driven by the cable tension

Received January 17, 2022; accepted July 28, 2022

rather than its compression [16]. Thus, each cable-driven link presents the unilateral actuating property.

To date, many studies have been performed to improve the CDPM's stiffness performance. For example, Yeo et al. [17] designed a CDPM involving tension resolution equipment that regulates the robot's stiffness. Bolboli et al. [18] investigated the feasible stiffness workspace to determine the allowable internal force range and increase the CDPM's stiffness. Anson et al. [19] proposed a tension factor to improve the quality of the wrench-closure workspace. However, the enhanced stiffness performance should be related to requirements of various application tasks. Using high cable tensions is one solution to produce high stiffness, but cable tensions are heavily dependent on the external force of the end effector. Overall, a lightweight design that can achieve the appropriate stiffness for cable-driven parallel systems is still challenging. On the basis of deficiencies of current methods, a cable-driven linear actuator (CDLA) capable of bidirectional motion and suitable for CDPM is presented in this study. The suggested CDLA scheme is lightweight and can realize high stiffness. Compared with the traditional cable-driven system, CDLA outputs the bidirectional motion by employing cable amplification and pulley systems.

The human masticatory system is a typical parallel architecture wherein the mandible is driven by a group of muscles working as an ensemble. Several bio-inspired parallel masticatory robots have already been designed. These robots can reproduce human chewing behavior in available applications, such as dental material testing, food texture evaluation, and performance testing of prosthesis and joint disc [20–23]. Additive manufacturing has progressed considerably in mandibular prosthesis and dental implant applications. Exploring new materials in the reconstruction of the temporomandibular joint (TMJ) disc is also an important research direction. Suitable biomaterials have been comprehensively explored and the structure has been improved for such applications. Performance testing, including *in vivo* and *in vitro* experiments, is a key step in the development of these oral and mandibular prostheses. Although *in vivo* implantation experiments need to be carried out on patients, they present disadvantages of high cost, high risk, and long cycle. *In vitro* experiments are convenient and can obtain detailed and quantitative analysis results. Figure 1 shows some typical *in vitro* performance testing applications of masticatory robots. Consequently, a masticatory robot that can realistically mimic human masticatory structure and behavior is suitable for *in vitro* performance testing.

Although many masticatory robots have been designed for different applications, they still suffer from a number of problems in reproducing human masticatory behavior. The Waseda Yamanashi (WY) robotic series is designed for dental training of jaw disorder patients [24,25], while the Waseda Jaw (WJ) series analyzes the relationship between jaw movement and resistance forces [26]. However, the WY robot fails to match with its human masticatory counterpart, and WJ robot presents only three degrees of freedom (DOFs). Notably, RSS (revolute–spherical–spherical, R: revolute, S: spherical)- [27] and PUS (prismatic–universal–spherical, P: prismatic, U: universal)-based [21,28] parallel mechanisms can mimic muscle motions on the basis of the physiological structure of the masticatory system. Parallel driving linkages are designed to follow each muscle's attach point position and action line. However, the muscle's origin position in these mechanisms changes with the linkage movement due to RSS and PUS linkage limitations, thereby affecting the output force direction of muscles. Recently, Lee et al. [29] designed a masticatory robot using a life-sized linear actuator that involves a cable providing the compressing force in one direction and a spring providing the stretching force in the opposite direction. As a result, the driving force in the stretching direction of the linear actuator is highly dependent on spring parameters. Chen et al. [30] designed a chewing robot to mimic the rhythmic motion of molars, but the robot presents only three DOFs.

The developed CDLA is further exploited to design a masticatory robot named Southeast University masticatory robot (SMAR) with six motors mounted on a fixed base in this study. Steel wires transmit the motion to the end effector through the CDLA with high stiffness and low inertia to satisfy the requirements of mimicking masticatory muscles without changing the muscle origin. Applying our CDLA to the masticatory robot can help reproduce human chewing behavior realistically.

The remainder of this paper is organized as follows. The concept of the stiffness amplification system and the design of the CDLA are introduced in Section 2. The detailed explanation of the masticatory robot, including mechanical design of the PUS linkage, temporomandibular joint, wire routing, and the whole robot, is presented in Section 3. The stiffness analysis and experimental verification of the CDLA are conducted in Section 4. Motion performance characteristics of the SMAR are verified through experimentation in Section 5. Finally, the conclusions of this work are drawn in Section 6.

2 CDLA with high stiffness

2.1 Basic concept

The CDLA generally relies on a cable and pulley system. The diagram of the system's pulling force amplification is presented in Fig. 2(a). Suppose the friction in this cable and pulley system is negligible, the number of cables turning around the movable pulleys is n (e.g., $n = 4$). The output force amplified by this "block and tackle" is expressed as follows:

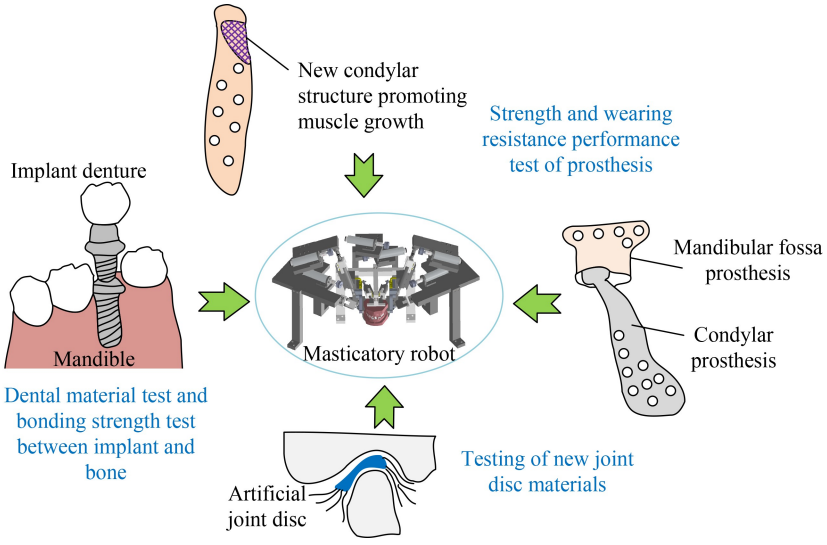

Fig. 1 Application areas of masticatory robot.

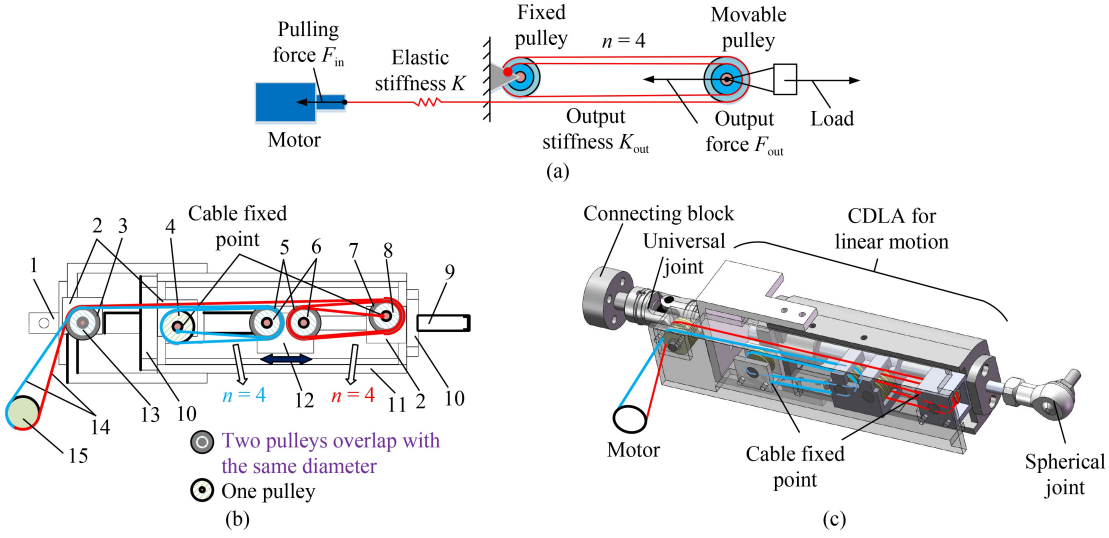

Fig. 2 New cable-driven linear actuator (CDLA): (a) diagram of the force and stiffness amplification, (b) diagram of the new CDLA with four cable parts (n = 4), and (c) UPS linkage based on the new CDLA (cables are omitted). 1–connecting block, 2–fixed block, 3–guide pulley A, 4–left fixed pulley, 5–movable pulley A, 6–movable pulley B, 7–fixed pulley A, 8–fixed pulley B, 9–sliding shaft, 10–linear bearing, 11–housing, 12–sliding block, 13–guide pulley B, 14–wire, 15–motor.

$$F_{out} = nF_{in}, \tag{1}$$

where F_{in} is the motor's input pulling force and F_{out} is the cable and pulley system's output force. The output stiffness of this pulley system (K_{out}) is expressed as follows:

$$K_{out} = \frac{F_{out}}{\Delta l_{out}} = \frac{nF_{in}}{\Delta l_{in}/n} = n^2 K, \tag{2}$$

where K is the cable's elasticity coefficient and Δl_{out} is the output deformation that is n times smaller than the input deformation Δl_{in}. Equation (2) highlights that the cable and pulley system amplifies the stiffness in a quadratic order. The reduction ratio is also n, the output force is n times the pulling force of a single cable, and the output stiffness is n^2 times the stiffness of a single cable. Notably, the transmission ratio and output stiffness can be changed by altering the number of pulleys and the cables' fixing point.

2.2 Mechanical design of the CDLA

A pair of cable and pulley systems (Section 2.1) are combined to form a bidirectional CDLA and achieve low inertia and high stiffness. As illustrated in Fig. 2(b), the number of cable parts n supporting the load is 4, with pulleys in different pattern fillings. According to the numerical notation of Fig. 2(b), a wire drives the two-block and tackle systems that comprise two sections representing one block and tackle system, that is, blue

and red sections. The red section is used as an example. The motor drives the fixed pulley A to rotate through the guide pulley A and utilize the red wire. The fixed pulley A is strapped on the fixed block on the right side to drive one movable pulley A, which is mounted on the sliding block. The wire drives the sliding block to translate in one direction after winding another fixed pulley B and another movable pulley B. The red wire is attached to the fixed point on the fixed block. The sliding shaft connected to the sliding block realizes the linear movement and output force and is carried by two linear bearings. Following the same principle, the motor can drive the sliding shaft to translate to another direction using the blue wire. The output force of the sliding shaft is four times the force of a single wire while the output stiffness is sixteen times the stiffness of a single wire when the interaction of these two block and tackle systems is ignored. The actual stiffness in the situation where two block and tackle systems interact is larger than this value. This phenomenon will be further discussed in Section 4.1.

The number of cable parts n supporting the load may alter. The number of cable parts n becomes three when the movable pulley on the sliding block is removed and the wire is attached to the sliding block. The output stiffness is nine times the stiffness of a single wire when the interaction of these two block and tackle systems is ignored. Therefore, the new CDLA addresses high output stiffness.

3 Design of the masticatory robot

3.1 Cable-driven UPS linkage

Driving devices of current masticatory robots are excessively large, and the driving direction is inconsistent with the muscle-force line of action. The form of driving with pulleys and cables was adapted to design the new CDLA to meet the requirements of small size, low inertia, and high stiffness and realize a compact masticatory robot. The proposed CDLA meets the masticatory robotic bionic requirements of size, line-of-muscle force action, and attachment point of the acting force. The CDLA structure of the developed masticatory robot is illustrated in Fig. 2(c), in which the numbered parts are consistent with those in Fig. 2(b). A spherical joint is installed on the sliding shaft and a universal joint is affixed on the connecting base to form a universal–prismatic–spherical (U<u>P</u>S) linkage, where the underscore indicates an active joint.

The motor is placed on a fixed platform. The comparison of the CDLA and the conventional linear actuator demonstrated the low mass and inertia of CDLA. Additionally, it acts as a speed reducer and presents amplified stiffness in the quadratic order. Finally, its low mass reduces the overall structural weight and achieves a driving device size closer to that of the human chewing muscle.

3.2 Masticatory robot with the CDLA

Figure 3 illustrates the mechanism diagrams of three existing masticatory robots to compare them against those of the developed one and highlight the benefits introduced by the CDLA further. For simplicity, only one driving linkage is shown in these mechanism diagrams. The swing motion of the crank suffers from an inconsistent direction of the driving force with the muscle-force line of action when the crank-actuated six-R<u>S</u>S parallel mechanism is considered [23,27] (Fig. 3(a)). The position of the upper muscle origin changes with the motion of the prismatic joint with consideration for the ball screw-driven six-P<u>U</u>S mechanism [21,28] (Fig. 3(b)). The actual driving-force line of action is inconsistent with the driving linkage motion between the masticatory robot and the human masticatory system. Chewing forces generated by these masticatory robots are different from those of the human masticatory process. A six-U<u>P</u>S parallel mechanism was proposed, in which the linear actuation involves the motor, reduction gear, and ball screw mounted on each linkage (Fig. 3(c)) [31,32]. Employing a linear actuation increases the volume of the actuator. These actuators for masseter and lateral pterygoid muscles could not be made within the specified length [32].

The proposed CDLA is small and light, with both ends fixed on the moving and fixed platforms. The comparison between the new actuator and the current ones is presented in Table 1. The CDLA structure solves the problem of a bulky driving linkage and swinging-muscle line of action. The corresponding mechanism diagram of one linkage of the new masticatory robot is illustrated in Fig. 3(d). Cable-driven U<u>P</u>S linkages in the new masticatory robot are designed to mimic the six main driving muscles of the human masticatory system. The connection of the universal joint and the fixed base indicates the maxilla's muscle attach point. Accordingly, the connection of the spherical joint and the moving platform indicates the mandible muscle attach point. The prismatic joint of the CDLA is driven by the motor placed on the fixed platform through a wire.

The new masticatory robot with the proposed CDLA is shown in Fig. 4. It involves three symmetrically distributed linkages corresponding to the three main human muscles, namely, masseter, temporalis, and lateral pterygoid. Positions of the universal and spherical joints are consistent with the muscle origin and insertion positions, while the actuation direction of the CDLA coincides with that of the resultant muscular force. Details on the origin and muscle insertion are discussed in a previous study [32]. The chewing force of the robot

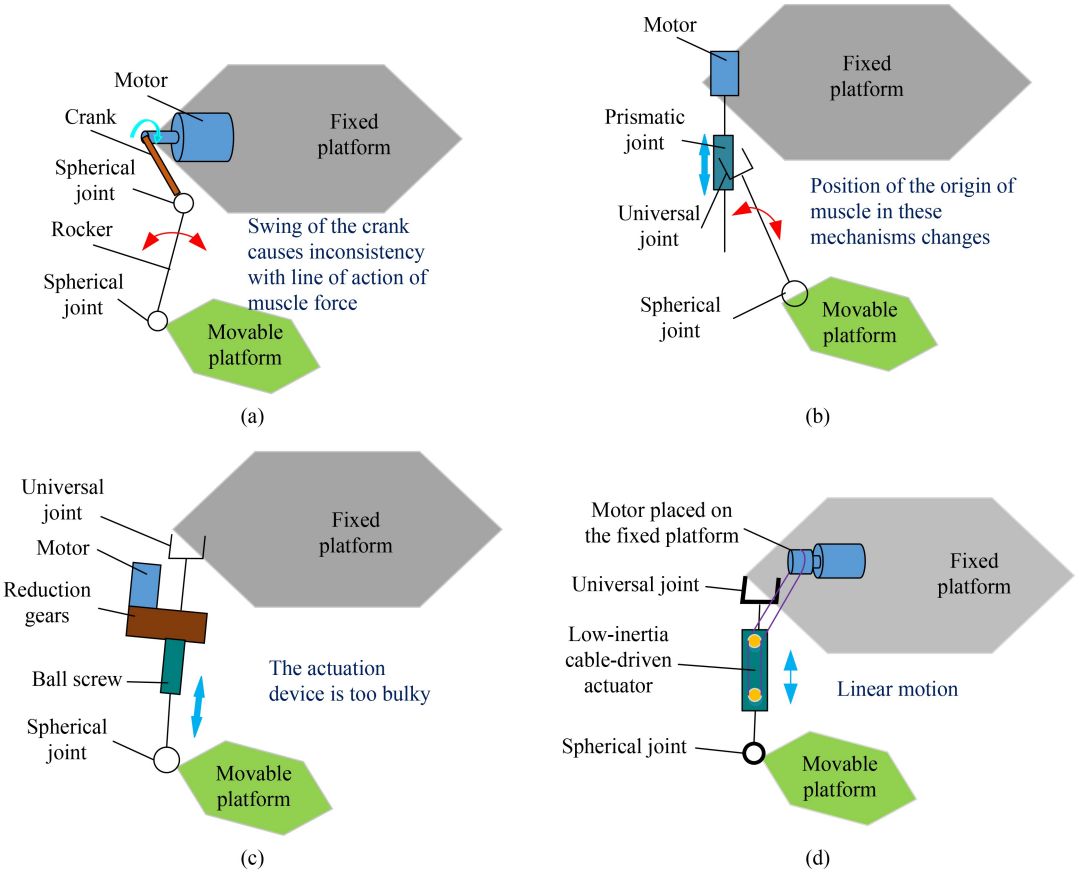

Fig. 3 Driving linkage in existing masticatory robots and the new one: (a) crank-actuated six-RSS mechanism, (b) ball screw-driven six-PUS mechanism, (c) ball screw-driven six-UPS mechanism, and (d) one driving linkage of the new masticatory robot.

Table 1 Comparison between the new actuator and the existing ones

Type of driving linkage	Location of motor and gear	Direction of the driving force and the muscle-force line of action	Weight of one linkage (moving parts)	Features
Crank-actuated six-RSS robot	On the fixed platform	Inconsistent; swing crank	Less than 80 g	Light; inconsistent force line
Ball screw-driven six-PUS robot	On the fixed platform	Inconsistent; muscle origins change	About 220 g	Heavy; inconsistent force line
Ball screw-driven six-UPS robot	On the linkage	Consistent	More than 260 g	Heavy; consistent force line
CDLA-based six-UPS robot	On the fixed platform	Consistent	Less than 90 g	Light; consistent force line

is expected to reach about 300 N, and the maximum opening angle is 35°.

Notably, the elevation of the mandible involves a powerful movement, with the power mainly provided by masseter and temporalis linkages. The lateral pterygoid linkage mainly accomplishes the protrusion movement of the mandible. The number of cable windings n for the masseter and temporalis linkages is equal to 4 to achieve powerful forces from the masseter and temporalis linkages and the compact size of the CDLA at the same time. n for the lateral pterygoid linkage is equal to 2 because the motion range and the output force of the lateral pterygoid are small.

3.3 Temporomandibular joint

TMJ is formed by articulating the temporal bone and the mandible and involves three surfaces, namely, condyle, fossa, and articular tubercle. The TMJ acts as a sliding hinge, where the condyle moves along the fossa surface to the articular tubercle to allow both the protrusion/retraction and elevation/depression movements of the mandible. The mandible can simultaneously rotate around the condylar head during this process. A condylar structure is fixed on the mandible of the proposed masticatory robot. Specifically, a fossa block is installed on the support, the ball head of the condylar structure is placed inside a cavity of the fossa block, and the surface of the cavity constrains the mandible's motion. The diagram of the TMJ structure is illustrated in Fig. 4(b).

3.4 Motor and wire guidance

The motor is mounted on the support base, and a wire

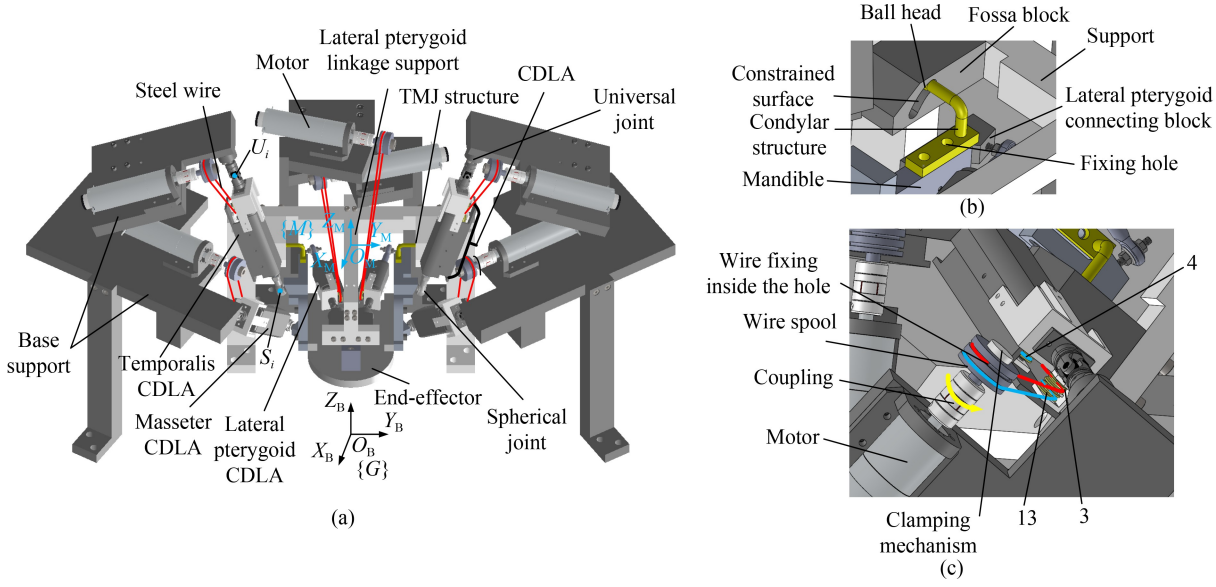

Fig. 4 Design of the masticatory robot with cable-driven linear actuator (CDLA): (a) three-dimensional model of the masticatory robot (U_i: universal joint, S_i: spherical joint), (b) structure diagram of the temporomandibular joint (TMJ) structure, and (c) top view of the wire winding.

spool is connected to the motor through a coupling. The two antagonistic wires exiting the CDLA are pretensioned via the clamping mechanism and go through two fixed holes on the wire spool. Assuming that the motor rotates in the direction of the yellow arrow shown in Fig. 4(c), the red wire tenses and the blue wire releases accordingly. The tensioned wire (red line) driven by the motor pulls the sliding shaft to extend outward. The sliding shaft slides in when the motor rotates in the opposite direction. Displacements of the two antagonistic wires are identical in motion given that the number n of cables turning around movable pulleys of the two cable-pulley systems in the CDLA is the same. The length of the wire can be adjusted to prevent slack and set the appropriate pretension through the clamping mechanism.

4 Stiffness analysis and performance validation of the CDLA

4.1 Stiffness analysis

The steel wire actuates the CDLA. Compared with the frame, sliding shaft, and motor, the wire is the most flexible component in the CDLA structure. However, calculating the stiffness and strength of the CDLA is necessary because the wire affects the CDLA. Friction is ignored in the following theoretical derivation because accurate friction is very difficult to model and linear and ball bearings are used in the CDLA to minimize the friction as extensively as possible.

The relationship between the motion of the sliding shaft and the wire is presented in Fig. 5. x denotes the distance

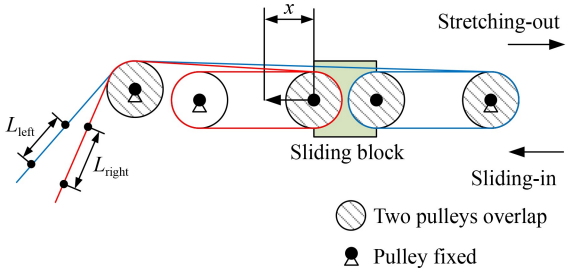

Fig. 5 Structural diagram of the cable-driven parallel manipulator.

that the sliding block moves, and L_{left} and L_{right} are the lengths of the left and right wires that pull or loosen, respectively. The relationship between the wire's amount of change and the sliding block's moving distance is expressed as follows:

$$L_{right} = -L_{left} = nx. \tag{3}$$

The following equation can be obtained using the virtual work concept:

$$F\Delta x = T_{pull}\Delta L - T_{loosen}\Delta L, \tag{4}$$

where F is the external force applied to the sliding shaft, T_{pull} is the tension of the pulled wire, T_{loosen} is the tension of the loosened wire during the movement, and Δx and ΔL are the infinitesimal changes of the moving distance of the sliding block and the length of wires, respectively. Assuming that the wire is pretensioned by a distance of L_{pre}, when an external force is applied to the sliding shaft, the tension T_{pull} of the pulled wire will be larger than the tension T_{loosen} of the loosened wire. T_{pull} and T_{loosen} can be calculated as follows:

$$T_{\text{pull}} = k_{\text{w}}(L_{\text{pre}} + \Delta L), \quad (5)$$

$$T_{\text{loosen}} = k_{\text{w}}(L_{\text{pre}} - \Delta L), \quad (6)$$

where k_{w} is the stiffness coefficient of wires.

The following equation can be derived after differentiating Eq. (3):

$$\frac{\Delta L}{\Delta x} = n. \quad (7)$$

Substituting Eq. (7) to Eq. (4) can express the relationship between the output force F and the cable tension as follows:

$$F = \frac{\Delta L}{\Delta x}(T_{\text{pull}} - T_{\text{loosen}}) = n(T_{\text{pull}} - T_{\text{loosen}}) = n\Delta T, \quad (8)$$

where $\Delta T = T_{\text{pull}} - T_{\text{loosen}}$ is the input force generated by the motor.

F can be calculated by substituting Eqs. (5) and (6)–(8) as follows:

$$F = n\Delta T = 2nk_{\text{w}}\Delta L = 2n^2 k_{\text{w}}\Delta x. \quad (9)$$

Hence, CDLA's stiffness (k_{la}) can be expressed as follows:

$$k_{\text{la}} = F/\Delta x = 2n^2 k_{\text{w}}. \quad (10)$$

Equations (8) and (10) show that the output force is n times the input force and CDLA's stiffness is $2n^2$ times the wire stiffness.

4.2 Performance validation

The CDLA structure (n = 4) and housing are fabricated via 3D printing technology. Nylon-coated steel wires were used for the CDLA's cable and pulley system (7 × 7 construction, diameter of 0.5 mm, and breaking strength of 143 N). Nine pulleys with bearings are used to decrease the friction of CDLA. The force transmission and stiffness performance of the CDLA structure are verified through experiments.

4.2.1 Force transmission

Two pull and push dynamometers (resolution of 0.01 N and maximum force of 55 N) are used to verify the force transmission performance of the CDLA (n = 4) and measure the input force of the wire and the output force of the sliding shaft. The relationship between the input force of the wire and the output force of the sliding shaft is illustrated in Fig. 6. We examine two cases, that is, the sliding shaft slides out and in, with the related motion direction shown in Fig. 5 in the experiments. The experimental results demonstrated that the amplified output force is lower than the theoretical value of four times the input force (Eq. (8)). The force transmission efficiency is defined as the ratio of the actual output force value to the theoretical output force value and corresponds to each input force plotted in the figures (red points shown in Fig. 6). Our experiments indicated that the average force transmission efficiency in the stretching-out and sliding-in directions is 84.5% and 85.9%, respectively.

The force transmission loss originates from the friction of pulleys and wires and the friction of the pulley bearing and linear bearings supporting the sliding shaft. The average force transmission efficiency in the sliding-in direction is more significant than that in the stretching-out direction because of another guiding pulley that increases friction in the stretching-out direction.

4.2.2 Stiffness performance

The CDLA (n = 4) is used for the masseter and temporalis linkages, and CDLA (n = 2) is utilized for the lateral pterygoid linkage. The stiffness performance of CDLAs (n = 4) and (n = 2) is verified through the experimental setup presented in Fig. 7(a). Two driving wires are fixed and pretensioned (30 N) to prevent slack. The pull–push dynamometer is adopted to apply forces to the CDLA, and a dial gauge (0.001 mm resolution) is

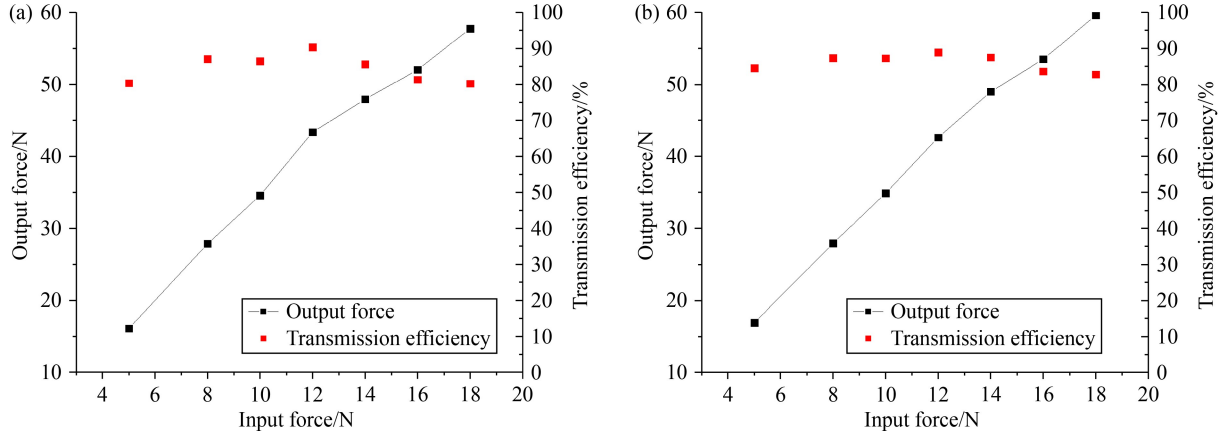

Fig. 6 Force transmission between output and input forces: (a) shaft stretching-out direction and (b) shaft sliding-in direction.

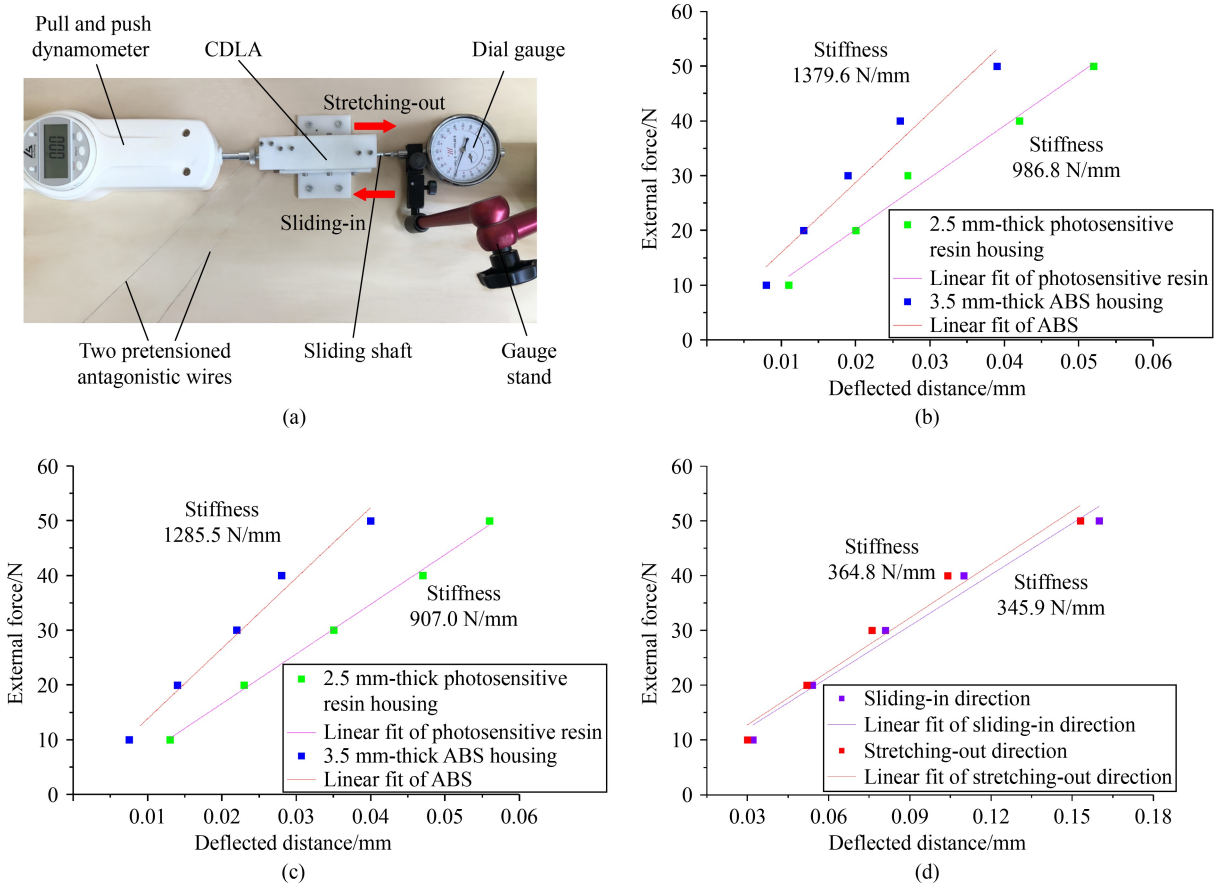

Fig. 7 Experimental setup and measured stiffness of the cable-driven linear actuator (CDLA): (a) experimental setup of the CDLA for stiffness measurement (n = 4); stiffness of the CDLA (b) n = 4 in the shaft stretching-out direction, (c) n = 4 in the shaft sliding-in direction, and (d) n = 2 with 3 mm-thick acrylonitrile butadiene styrene in two directions.

fixed on a gauge stand to measure the deflected displacement of the sliding shaft.

The wire's measured stiffness k_w is 64.5 N/mm, with the theoretical CDLA stiffness k_{la} equals to 2064 N/mm based on Eq. (10) when n = 4. The first experiment was carried out on the CDLA with a housing made of 2.5 mm-thick photosensitive resin material. Green dots in Figs. 7(b) and 7(c) illustrate the external forces and the measured deflected distances when the shaft slides out and in. The CDLA (n = 4) stiffness is calculated with a linear fit under the two cases, as denoted by the purple line in Figs. 7(b) and 7(c). The measured stiffnesses for the stretching-out and sliding-in directions are 986.8 and 907.0 N/mm, respectively. The actual stiffness is slightly smaller than half the theoretical value. The reduction of CDLA's stiffness is due to the flexibility of the housing frame. A thicker housing was fabricated with 3.5 mm-thick acrylonitrile butadiene styrene (ABS) material to verify this phenomenon. The measured deflected distances of the shaft are shown in Figs. 7(b) and 7(c). The red line demonstrates that the stiffness of the CDLA rises significantly. The stiffnesses for the stretching-out and sliding-in directions reach 1379.6 and 1285.5 N/mm, respectively. The stiffness can increase to about 21.4 times the input wire stiffness when n = 4 under this experiment condition. Notably, the stiffness can be improved further through the use of material with high strength for the frame. The stiffness of CDLA significantly improves compared with that of the traditional cable-driven system.

The lateral pterygoid linkage of the masticatory robot uses the CDLA with n = 2 for the actuator. The stiffness performance of the CDLA (n = 2) was also verified. The theoretical CDLA stiffness k_{la} is 516 N/mm based on Eq. (10) when n = 2. The housing of the CDLA is fabricated using 3 mm-thick ABS. Deflected distances of the shaft in two directions corresponding to different external forces are shown in Fig. 7(d). The stiffnesses for the stretching-out and sliding-in directions reach 364.8 and 345.9 N/mm, respectively. Although the stiffness value when n = 2 is smaller than that when n = 4, it still increases approximately 5.7 times compared with the input wire stiffness. The CDLA exerts a significant stiffness amplification effect compared with the traditional cable-driven system. A large n corresponds to a strong amplification effect. Meanwhile, the CDLA presents another advantage of bidirectional motion.

5 Control and experiment of the masticatory robot

5.1 Prototype of the masticatory robot

A bio-inspired masticatory robot adopting a human parallel masticatory system is designed. Figure 8 presents the SMAR prototype. The robot's components are machined using aluminum alloy, except for the six CDLAs. Each CDLA is driven by a 40 W MAXON ECX26L motor with GPX26A gears (35:1). We utilize two cable parts (n = 2) rotating the movable pulley of the lateral pterygoid CDLA given that the protrusion movement accomplished by the lateral pterygoid and the required force of this muscle are both small. The motion range of the lateral pterygoid CDLA is 13 mm. The temporalis and masseter mainly engage the mouth-opening movement. The number of cable parts n is set as 4 for these CDLAs given that the required forces of these muscles are both large. Motion ranges of both the temporalis CDLA and the masseter CDLA are 25.5 mm.

The programmable multiaxis controller CK3M-CPU121 by OMRON is used to control the robot, and six drivers by DiGE Inc. are employed to drive the corresponding motors through EtherCAT. An upper computer is connected with the multiaxis controller to calculate the inverse kinematics of the robot and send control instructions. The six multiaxis controllers are set to work in the position control mode.

5.2 Inverse kinematics and trajectory planning

The established coordinate system of the robot is presented in Fig. 4(a). The mandible frame $\{M\}$ is attached to the middle of the line between the two ball heads of the left and right TMJ structure, while the global frame $\{G\}$ is fixed on the base directly under the mandible frame. U_i and S_i (i = 1,2,…,6) are the respective origin and insertion points of the six-muscle CDLA.

The vector of each CDLA $\boldsymbol{U}_i\boldsymbol{S}_i^G$ (i = 1,2,…,6) in frame $\{G\}$ can be expressed as

$$\boldsymbol{U}_i\boldsymbol{S}_i^{\,G} = \boldsymbol{S}_i^G - \boldsymbol{U}_i^G = \left(\boldsymbol{p}^G + \boldsymbol{R}_M^G\boldsymbol{S}_i^M\right) - \boldsymbol{U}_i^G, \tag{11}$$

where $\boldsymbol{p}^G$ is the position of $\{M\}$ relative to $\{G\}$, $\boldsymbol{S}_i^M$ is the coordinate of S_i with respective to $\{M\}$, $\boldsymbol{U}_i^G$ and $\boldsymbol{S}_i^G$ are the coordinate of U_i and S_i with respective to $\{G\}$, respectively, and $\boldsymbol{R}_M^G$ is the rotation transformation matrix mapping from $\{M\}$ to $\{G\}$. The rotation transformation matrix can be expressed as follows given the roll–pitch–yaw angles (α, β, γ):

$$\boldsymbol{R}_M^G = \begin{bmatrix} c\gamma c\beta & -s\gamma c\alpha + c\gamma s\beta s\alpha & s\gamma s\alpha + c\gamma s\beta c\alpha \\ s\gamma c\beta & c\gamma c\alpha + s\gamma s\beta s\alpha & -c\gamma s\alpha + s\gamma s\beta c\alpha \\ -s\beta & c\beta s\alpha & c\beta c\alpha \end{bmatrix}, \tag{12}$$

where s and c indicate the sine and cosine functions, respectively. The corresponding length of each CDLA ($l_{U_iS_i}$) can be calculated as follows when a desired position and orientation is given:

$$l_{U_iS_i} = \left\|\boldsymbol{U}_i\boldsymbol{S}_i^{\,G}\right\|. \tag{13}$$

Chewing is an essential functional motion in masticatory robots. The end effector of SMAR is constrained by two TMJ structures on each side of the robot (Figs. 4(a) and 4(b)) to realize a four-DOF motion. Assume that frame $\{M_0\}$ coincides with frame $\{M\}$ when the mandible is in the home position. Curves of constrained surfaces concerning frame $\{M_0\}$ can be described as

$$Z = -0.07X^2 - 0.2X,\ 0 \leqslant X \leqslant 10, \tag{14}$$

where X and Z are the coordinate of the curves in frame $\{M_0\}$.

Constrained motions of TMJ structures in Y direction are $-75.67 \leqslant Y_{\mathrm{L}} \leqslant -70.67$ and $70.67 \leqslant Y_{\mathrm{R}} \leqslant 75.67$, where

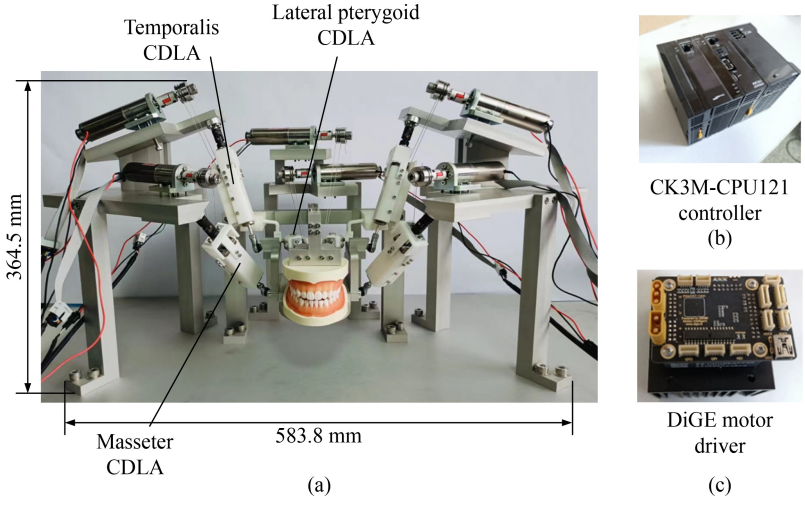

Fig. 8 Southeast University masticatory robot: (a) prototype of the robot, (b) controller, and (c) driver.

Y_L and Y_R represent the coordinates of the left and right ball heads in the TMJ structure, respectively (Fig. 4(b)). We plan the desired trajectory of the first molar of the lower jaw while considering geometric constraints of TMJ structures and the kinematics model of the robot to perform the chewing movement experiment on the SMAR. As shown in Fig. 9, the first molar on the lower jaw opens to 11.45 mm in the vertical direction and 3.4 mm in the horizontal direction in one chewing cycle.

5.3 Chewing experiment

5.3.1 Chewing motion

The encoder ENX10 EASY with a resolution of 1024 pulse/revolution (p/r) is used in the motor. The diameter of the wire spool is 9.75 mm, and the calculated resolution of wire length changes can reach 0.0017 mm. The robot in the chewing experiment is controlled to track the chewing trajectory presented in Fig. 9 during each chewing cycle with a period of 1.1 s. The corresponding snapshots showing the robot during the chewing movement are presented in Figs. 10(a) and 10(b). Displacements and velocities of the six wires according to the encoder's measurements are illustrated in Figs. 10(c) and 10(d). These two figures indicated that the masseter CDLA presents a large displacement and the lateral pterygoid shows a small displacement. The left masseter CDLA presents a maximum displacement of 13.23 mm and a maximum velocity of 41.12 mm/s. Our experimental results demonstrated that the robotic movement is consistent with human mandibular muscles. Hence, the effective control of the new CDLA allows the SMAR to achieve a natural human-like chewing motion.

5.3.2 Chewing force

The chewing force of the masticatory robot can be generated by placing simulated food with a certain thickness between the teeth. A diaphragm pressure sensor is used to measure the chewing force. The sensor head was placed between two circular polyethylene sheets to improve the measurement accuracy. The sensor sandwiched by polyethylene sheets was then placed between the upper and lower molars, as shown in Fig. 11(a). Chewing forces that correspond to two different thickness sheets were recorded during the occlusal phase when the lower jaw of the masticatory robot closed to the occlusal phase. Figures 11(b) and 11(c) present that the average chewing force is 102.6 N when the thickness of the polyethylene sheet is 1 mm while the average force reaches 171.5 N when the thickness of the sheet is 2 mm. The peak value of the chewing force reaches 234.2 N. Various chewing forces can be obtained by adjusting the bite depth of the masticatory robot's teeth to satisfy the performance test of dental material or prosthesis in a dynamic loading experiment.

6 Conclusions

A novel CDLA with bidirectional motion and low inertia is presented in this study to transmit motion with high stiffness and strength using a cable and pulley amplification mechanism. The mechanical design of the CDLA with four and two cable parts is presented. These parts are then exploited in a configuration involving six CDLAs and two TMJ structures to develop a masticatory robot named SMAR. The use of the new CDLA allows the small-sized and lightweight driving linkage of the SMAR

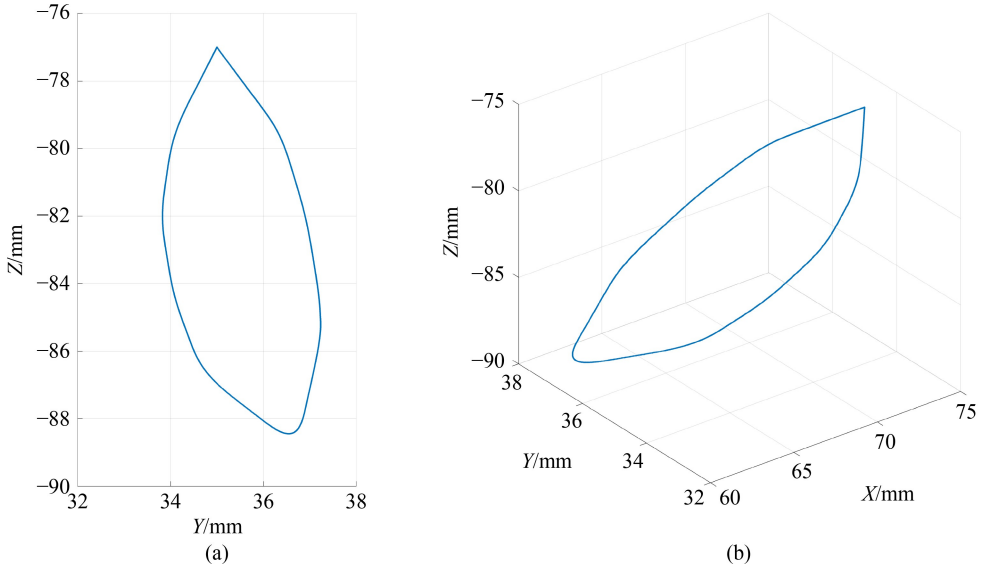

Fig. 9 Planned trajectory of the lower first molar in (a) the *YZ* plane and (b) the 3D space.

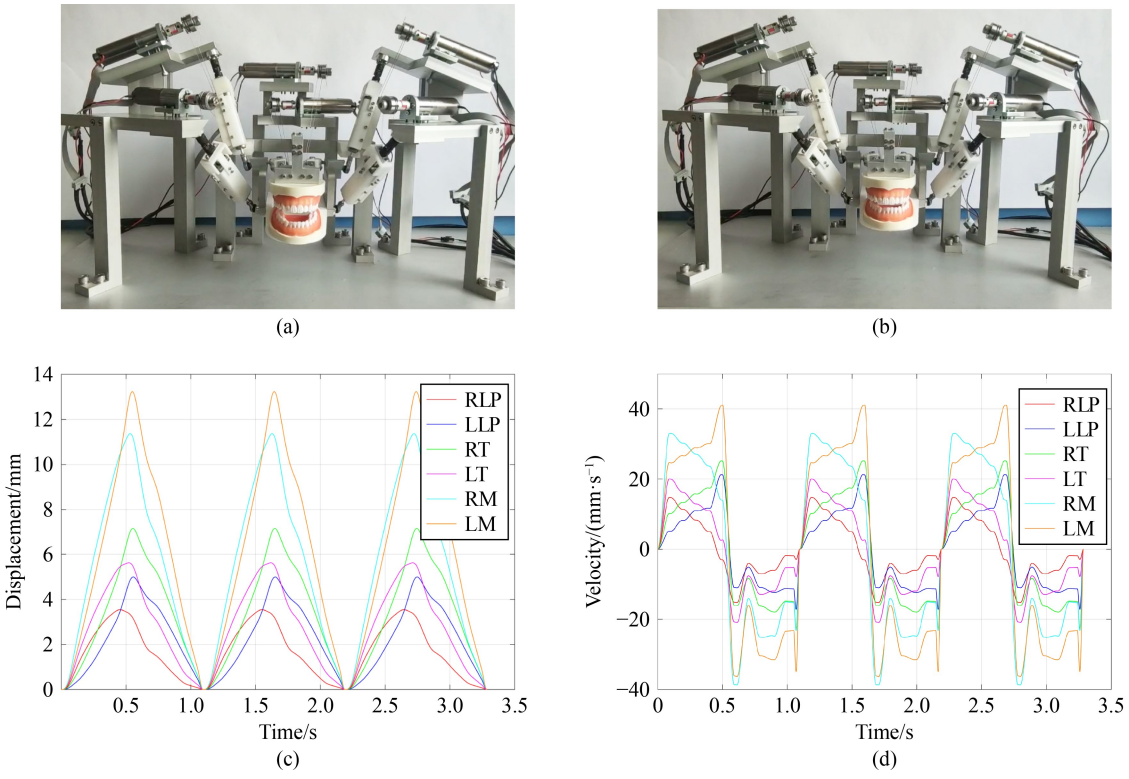

Fig. 10 Snapshots of the chewing movement and displacement and velocity trajectories of the six CDLAs: (a) opening movement, (b) closing movement, (c) displacements of the six CDLAs, and (d) velocities of the six CDLAs. RLP: right lateral pterygoid, LLP: left lateral pterygoid, RM: right masseter, LM: left masseter, RT: right temporalis, LT: left temporalis.

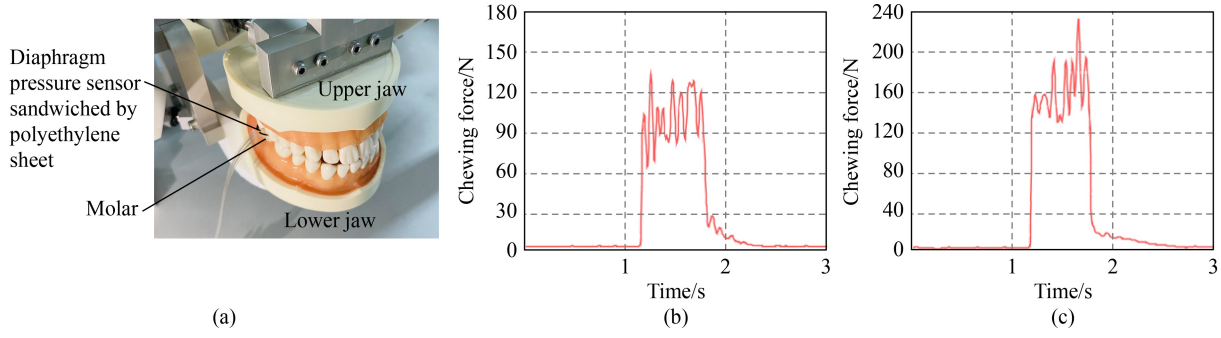

Fig. 11 Chewing force of the robot: (a) setup of the sensing system; chewing force corresponding to the (b) 1 mm-thick sheet and (c) 2 mm-thick sheet.

to output push and pull forces effectively. Compared with that of current masticatory robots, the position of the muscle origin remains unchanged during the movement of the mandible platform of SMAR, thereby enabling our proposed masticatory robot to reproduce human chewing more realistically.

Our stiffness analysis demonstrated that the stiffness amplification can reach $2n^2$ times the wire stiffness due to the proposed cable and pulley amplification mechanism. Force transmission and stiffness experiments indicated that the force transmission efficiency of the CDLA (n = 4) in the stretching-out and sliding-in directions is 84.5% and 85.9%, respectively. Accordingly, the measured stiffness for the CDLA (n = 4) in the two directions is 1379.6 and 1285.5 N/mm, respectively. The maximum stiffness amplification is 21.4 times the input wire stiffness under the experimental condition of this work. Overall, the experiments demonstrated that the stiffness of the new CDLA significantly improves. A prototype masticatory robot is developed and chewing experiments are conducted on the basis of the performance of CDLA to prove that typical chewing motion can be realized with the control of six CDLAs. Notably, the measured displacements and velocities of CDLAs verified that the developed masticatory robot can reproduce mandible motions. Chewing forces of the teeth during the chewing

motion can reach 234.2 N, thereby indicating satisfactory dynamic loading output capacity of the masticatory robot for the performance test of dental material or prosthesis.

Future investigations intend to focus on extending the CDLA's applicability to structures that demand high stiffness, low weight, and compact size given the satisfactory performance of the CDLA. The cable-driven redundantly actuated parallel mechanism and friction compensation dynamic feedforward control strategy of the robot will also be subjected to stiffness analysis. At present, the elastic property of the disc in the human TMJ is ignored despite its significant influence on the chewing force. However, rigid contact for the TMJ is commonly used in existing masticatory robots. Finally, we will also attempt to develop a new design for the TMJ structure while considering the constraints of both the disc and the ligament.

Nomenclature

Abbreviations

3D	Three dimensional
ABS	Acrylonitrile butadiene styrene
c, s	sine and cosine functions, respectively
CDLA	Cable-driven linear actuator
CDPM	Cable-driven parallel manipulator
DOF	Degree of freedom
PUS	Prismatic−universal−spherical
RSS	Revolute−spherical−spherical
SMAR	Southeast University masticatory robot
TMJ	Temporomandibular joint
WJ	Waseda Jaw
WY	Waseda Yamanashi
UPS	Universal−prismatic−spherical

Variables

F	External force applied to the sliding shaft
F_{in}	Motor's input pulling force
F_{out}	Cable and pulley system's output force
k_{la}	CDLA's stiffness
k_{w}	Stiffness coefficient of wires
K	Cable's elasticity coefficient
K_{out}	Output stiffness of this pulley system
Δl_{in}	Input deformation
Δl_{out}	Output deformation
$l_{U_iS_i}$	Corresponding length of each CDLA
L_{left}, L_{right}	Length of the left and right wires that pull or loosen, respectively
L_{pre}	Pretensioned distance of the wire
ΔL	Infinitesimal change of the length of wires
n	Number of cables turning around the movable pulleys
$\boldsymbol{p}^G$	Position of $\{M\}$ relative to $\{G\}$
$\boldsymbol{R}_M^G$	Rotation transformation matrix mapping from $\{M\}$ to $\{G\}$
S_i (i = 1, 2, …, 6)	Insertion points of the six-muscle CDLA
T_{loosen}	Tension of the loosened wire during the movement
T_{pull}	Tension of the pulled wire during the movement
ΔT	Input force generated by the motor
U_i (i = 1, 2, …, 6)	Origin points of the six-muscle CDLA
$\boldsymbol{U}_i\boldsymbol{S}_i^G$	Vector of each CDLA connecting point U_i and S_i
x	Distance that the sliding block moves
X	Coordinates in X direction
Δx	Infinitesimal change of the moving distance of the sliding block
Y_{L}, Y_{R}	Coordinates of the left and right ball heads in the TMJ structure, respectively
Y	Coordinates in Y direction
Z	Coordinates in Z direction
α, β, γ	Euler angles rotated about X, Y, and Z axes, respectively

Acknowledgements This work was supported by the Natural Science Foundation of Jiangsu Province, China (Grant No. BK20190368), the National Natural Science Foundation of China (Grant No. 51705063), the Fundamental Research Funds for the Central Universities, and Zhishan Scholar Program of Southeast University, China. The authors declare no conflict of interest.

References

1. Sun G F, Kleeberger M, Liu J. Complete dynamic calculation of lattice mobile crane during hoisting motion. Mechanism and Machine Theory, 2005, 40(4): 447–466
2. Tolles B A. US Patent, 20010034290A1, 2000-10-25
3. Sollmann K S, Jouaneh M K, Lavender D. Dynamic modelling of a two-axis, parallel, H-frame-type *XY* positioning system. IEEE/ASME Transactions on Mechatronics, 2010, 15(2): 280–290
4. Youssef K, Otis M J D. Reconfigurable fully constrained cable driven parallel mechanism for avoiding interference between cables. Mechanism and Machine Theory, 2020, 148: 103781
5. Geng X Y, Li M, Liu Y F, Li Y Y, Zheng W, Li Z B. Analytical tension-distribution computation for cable-driven parallel robots using hypersphere mapping algorithm. Mechanism and Machine Theory, 2020, 145: 103692
6. Abdolshah S, Zanotto D, Rosati G, Agrawal S K. Optimizing stiffness and dexterity of planar adaptive cable-driven parallel robots. Journal of Mechanisms and Robotics, 2017, 9(3): 031004
7. Zhang Z K, Shao Z F, Wang L P. Optimization and

implementation of a high-speed 3-DOFs translational cable-driven parallel robot. Mechanism and Machine Theory, 2020, 145: 103693
8. Zi B, Wang N, Qian S, Bao K L. Design, stiffness analysis and experimental study of a cable-driven parallel 3D printer. Mechanism and Machine Theory, 2019, 132: 207–222
9. Cui X, Chen W H, Jin X, Agrawal S K. Design of a 7-DOF cable-driven arm exoskeleton (CAREX-7) and a controller for dexterous motion training or assistance. IEEE/ASME Transactions on Mechatronics, 2017, 22(1): 161–172
10. Zanotto D, Rosati G, Minto S, Rossi A. Sophia-3: a semiadaptive cable-driven rehabilitation device with a tilting working plane. IEEE Transactions on Robotics, 2014, 30(4): 974–979
11. Hu X H, Chen A, Luo Y G, Zhang C, Zhang E. Steerable catheters for minimally invasive surgery: a review and future directions. Computer Assisted Surgery, 2018, 23(1): 21–41
12. Sanjuan J D, Castillo A D, Padilla M A, Quintero M C, Gutierrez E E, Sampayo I P, Hernandez J R, Rahman M H. Cable driven exoskeleton for upper-limb rehabilitation: a design review. Robotics and Autonomous Systems, 2020, 126: 103445
13. Gao B T, Zhu Z Y, Zhao J G, Jiang L J. Inverse kinematics and workspace analysis of a 3 DOF flexible parallel humanoid neck robot. Journal of Intelligent & Robotic Systems, 2017, 87(2): 211–229
14. Chen X B, Yao J T, Li T, Li H L, Zhou P, Xu Y D. Development of a multi-cable-driven continuum robot controlled by parallel platforms. Journal of Mechanisms and Robotics: Transactions of the ASME, 2021, 13(2): 1–11 (in Chinese)
15. Yuan H, Courteille E, Deblaise D. Static and dynamic stiffness analysis of cable-driven parallel robots with non-negligible cable mass and elasticity. Mechanism and Machine Theory, 2015, 85: 64–81
16. Qian S, Zi B, Shang W W, Xu Q S. A review on cable-driven parallel robots. Chinese Journal of Mechanical Engineering, 2018, 31(1): 66
17. Yeo S H, Yang G, Lim W B. Design and analysis of cable-driven manipulators with variable stiffness. Mechanism and Machine Theory, 2013, 69: 230–244
18. Bolboli J, Khosravi M A, Abdollahi F. Stiffness feasible workspace of cable-driven parallel robots with application to optimal design of a planar cable robot. Robotics and Autonomous Systems, 2019, 114: 19–28
19. Anson M, Alamdari A, Krovi V. Orientation workspace and stiffness optimization of cable-driven parallel manipulators with base mobility. Journal of Mechanisms and Robotics, 2017, 9(3): 031011
20. Xu W L, Bronlund J E. Mastication Robots: Biological Inspiration to Implementation. Berlin: Springer, 2010
21. Wen H Y, Cong M, Wang G F, Qin W L, Xu W L, Zhang Z S. Dynamics and optimized torque distribution based force/position hybrid control of a 4-DOF redundantly actuated parallel robot with two point-contact constraints. International Journal of Control, Automation and Systems, 2019, 17(5): 1293–1303
22. Kasper R, Winter K, Pietzka S, Schramm A, Wilde F. Biomechanical in vitro study on the stability of patient-specific CAD/CAM mandibular reconstruction plates: a comparison between selective laser melted, milled, and hand-bent plates. Craniomaxillofacial Trauma & Reconstruction, 2021, 14(2): 135–143
23. Mostashiri N, Dhupia J, Verl A, Bronlund J, Xu W L. Optimizing the torque distribution of a redundantly actuated parallel robot to study the temporomandibular reaction forces during food chewing. Journal of Mechanisms and Robotics, 2020, 12(5): 051008
24. Takanobu H, Takanishi A, Ozawa D, Ohtsuki K, Ohnishi M, Okino A. Integrated dental robot system for mouth opening and closing training. In: Proceedings of 2002 IEEE International Conference on Robotics and Automation. Washington: IEEE, 2002, 1428–1433
25. Takanobu H, Maruyama T, Takanishi A, Ohtsuki K, Ohnishi M. Mouth opening and closing training with 6-DOF parallel robot. In: Proceedings of IEEE International Conference on Robotics and Automation. San Francisco: IEEE, 2000, 1384–1389
26. Takanobu H, Takanishi A, Kato I. Design of a mastication robot mechanism using a human skull model. In: Proceedings of 1993 IEEE/RSJ International Conference on Intelligent Robots and Systems. Yokohama: IEEE, 1993, 203–208
27. Xu W L, Torrance J D, Chen B Q, Potgieter J, Bronlund J E, Pap J S. Kinematics and experiments of a life-sized masticatory robot for characterizing food texture. IEEE Transactions on Industrial Electronics, 2008, 55(5): 2121–2132
28. Wen H Y, Cong M, Xu W L, Zhang Z S, Dai M. Optimal design of a linkage–cam mechanism-based redundantly actuated parallel manipulator. Frontiers of Mechanical Engineering, 2021, 16(3): 451–467
29. Lee S J, Kim B K, Chun Y G, Park D J. Design of mastication robot with life-sized linear actuator of human muscle and load cells for measuring force distribution on teeth. Mechatronics, 2018, 51: 127–136
30. Chen B X, Dhupia J S, Morgenstern M P, Bronlund J E, Xu W L. Development of a biomimetic masticating robot for food texture analysis. Journal of Mechanisms and Robotics, 2022, 14(2): 021012
31. Xu W L, Pap J S, Bronlund J. Design of a biologically inspired parallel robot for foods chewing. IEEE Transactions on Industrial Electronics, 2008, 55(2): 832–841
32. Xu W L, Bronlund J, Kieser J. Choosing new ways to chew: a robotic model of the human masticatory system for reproducing chewing behaviors. IEEE Robotics & Automation Magazine, 2005, 12(2): 90–100